




Freeze casting of lamellar-structured porous lead-free $(\text{Na}_{0.52}\text{K}_{0.48})(\text{Nb}_{0.95}\text{Sb}_{0.05})\text{O}_3$ piezoceramic with remarkable enhancement in piezoelectric voltage constant and hydrostatic figure of merit

Prashant Dixit^{1,2}, Shaurya Seth³, Bhupender Rawal¹, B. Praveen Kumar^{1,*}, and Himanshu Sekhar Panda^{2,*} 

¹Armament Research and Development Establishment, Pune 411021, India

²Sustainable Energy Laboratory, Department of Metallurgical and Materials Engineering, Defence Institute of Advanced Technology, Pune 411025, India

³National Institute of Technology Karnataka, Surathkal 575025, India

Received: 2 November 2020

Accepted: 5 January 2021

Published online:
12 February 2021

© The Author(s), under exclusive licence to Springer Science+Business Media, LLC part of Springer Nature 2021

ABSTRACT

The study reports the development of lamellar-structured, porous lead-free $(\text{Na}_{0.52}\text{K}_{0.48})(\text{Nb}_{0.95}\text{Sb}_{0.05})\text{O}_3$ ceramics, abbreviated as NKNS, using the freeze-casting method with water as pore-forming agent. The effect of directional porosity on the microstructure, dielectric, and piezoelectric properties of the lead-free porous material is investigated. Furthermore, the effects of conventional and microwave sintering on microstructure and piezoelectric properties have also been analyzed. In addition, the study compares conventional and corona poling too. The results depicted no deterioration of piezoelectric properties (d_{33} : 130 pC/N), despite being ~ 50% porosity, along with reasonably good hydrostatic piezoelectric strain coefficient (d_h : 60 pC/N). The samples exhibited hydrostatic piezoelectric voltage coefficient (g_h) of 58.70 mV.m/N providing a significant value of the hydrostatic figure of merit (HFOM = $d_h \cdot g_h$: $3522 \times 10^{-15} \text{ Pa}^{-1}$) for the porous NKNS ceramic which is nearly 39 times more than the dense ceramic. Considering its unique advantages such as environmental friendly, less dense, wide performance range with enhanced figure of merit, the lamellar-structured NKNS ceramic is a promising material for sensor and transducer applications.

Address correspondence to E-mail: praveenkumar@arde.drdo.in; himanshusp@diat.ac.in; hspanda3@gmail.com

1 Introduction

Piezoelectric materials, especially PZT based, have been used widely as hydrophones, projectors, FeRAM, and actuators due to their optimal piezoelectric properties and adaptability in terms of the variety of macro- and micro-scale fabrication methods [1, 2]. However, as the PZT-based materials are toxic due to lead, the world is trying to curtail its use. The European Union has even adopted the directive on restricting the use of certain speculative substances in electrical and electronic equipment in 2003 [3]. Recently, comprehensive piezoelectric performance and practical applications in BCZT-based [4] and BNKT-based [5] lead-free materials are studied. Therefore, lead-free piezoceramics are drawing the attention of researchers.

Porous piezoceramics are of special interest as they have several possible benefits over dense piezoceramics. When used underwater, the high density, relative permittivity, and low values of d_{31} , as well as g_{31} of dense piezoelectric ceramics, are unfavorable as it leads to high acoustic impedance and low hydrostatic figure of merit (HFOM) which, in turn, reduces the overall performance of the transducer devices [6]. In general, these parameters determine the actuating capability, sensitivity, and suitability of ceramics required for electronic applications. Therefore, porous piezoelectric ceramics are preferable because of low acoustic impedance and high hydrostatic figure of merit, achieved due to the less volume fraction of the active ceramic phase [7]. Piezoelectric porous ceramics can be considered a unique case of composites as porosity (air) is usually reflected as a secondary phase. These materials demonstrate excellent coupling with water and human tissues and are, therefore, used widely in low-frequency hydrophones [8], pressure and shear sensors [9], medical diagnostics [10], and non-destructive testing [11, 12].

Porous piezoceramics have been developed by various fabrication techniques like burnable plastic sphere process (BURPS) [13, 14], foam reticulation [15], replica method [16], freeze casting using tert-butyl alcohol and camphene [17, 18], solid freeform fabrication (SFF) [19], and replamine process [20]. Out of all the processes, the freeze-casting route has many unique advantages compared with other preparation methods of porous ceramics: environment-friendly process, fast manufacturing, low material waste, little post-machining, no drying

cracks, essentially zero shrinkage, and no complicated binder burnout process [21].

Solid loading, pores size, and wall thickness play a decisive role in determining porous ceramics ultimate properties [22]. Xie et al. reported a unique combination of flexible and highly active self-powered force sensor arrays of PZT ceramics with highly aligned pore channels prepared by water-based freeze-casting process [9]. Guo et al. fabricated 1–3 type porous PZT-5H ceramic by tert-butyl alcohol-based unidirectional freeze-casting method to achieve the peak value of HFOM ($9648 \times 10^{-15} \text{ Pa}^{-1}$) and the lowest value of the acoustic impedance (1.3 MRayls) which can be useful for medical imaging [17]. The introduction of aligned porosity by freeze casting improved energy-harvesting and pyroelectric-sensing ability of porous PZT ceramics [23].

In lead-free piezoceramics, Qi Wang et al. were the first to study the effect of porosity on lead-free LNKN composition for bio-applications [24–26]. Lead-free micro-honeycomb barium titanate (BaTiO_3) ceramics were studied, and the special porous structure achieved by freeze casting was beneficial to the domain rotation during polarization [27]. Roscow et al. showed the possible use of freeze-cast porous barium titanate samples with 45 vol% porosity for energy-harvesting applications [28]. The construction of a lamellar ceramic architecture is an effective method to obtain high dielectric properties and energy density of composites which can be used to design improved energy storage materials and is promising for the application of dielectric composites in modern electrical and electronic industries [29]. Recently, NKN-based porous lead-free piezoceramic has been prepared by a hot-pressing method that displayed a stable piezoelectric charge coefficient (d_{33}) of 100 pC/N within a wide range of porosity [30].

In porous piezoceramics, controlling the volume fraction of porosity with uniform, defect-free microstructures is more important than the ability to produce specific pore sizes [14]. Depending upon the freezing medium, freeze casting may be utilized to induce different connectivity in composites. Ice templating produces a highly oriented porous structure exhibiting 2–2 connectivity of the active (piezoelectric ceramic) phase and the passive (pore) phase along with the freezing directions. Due to lamellar structure and 2–2 connectivity along with the freezing and poling directions, the material may exhibit a

mechanical strength as higher as three times as conventional porous structures, and figure of merit 2 to 3 times higher than the dense counterpart with partial improvement in fracture toughness has been reported [31, 32].

Inspired by this, we have endeavored to develop and characterize the ice-templated lamellar-structured porous lead-free piezoceramics by freeze-casting method. As per our survey, currently, there are no studies available on the same. This study has fabricated environment-friendly porous lamellar-structured lead-free piezoceramics with highly aligned porosity to produce high-performance materials for piezoelectric underwater applications. The study also elaborates on the effects of different poling methods (corona vs. silicon oil bath) and sintering methods (conventional vs. microwave) on the piezoelectric properties. The pore structure and pore morphology are observed, and properties are evaluated to demonstrate the effects of porosity on dielectric and piezoelectric properties such as ϵ_r , d_{33} , d_{31} , d_{11} , g_{11} , and HFOM of porous lead-free NKNS ceramics. Furthermore, the study also compares the piezoelectric properties of the developed porous ceramics with the dense NKNS ceramics.

2 Experimental

The lead-free $(\text{Na}_{0.52}\text{K}_{0.48})(\text{Nb}_{0.95}\text{Sb}_{0.05})\text{O}_3$ ceramic powder, hereafter abbreviated as NKNS, was produced by a conventional solid-state reaction method as discussed in our previous studies [33, 34]. The NKNS powder was dispersed in deionized water to form a suspension with solid loading of 70 weight percent with 1 weight percent dispersant (Darwan C-ammonium poly-methacrylate) and 2 weight percent binder (poly vinyl alcohol). The suspension was ball milled for 24 h using zirconia-grinding media in high-density polyethylene bottles. Defoamer was added after 2 h of ball milling. The homogeneous slurry so prepared was degassed under vacuum for 5 min by using a magnetic stirrer. The degassed slurry was poured into pre-cooled (Teflon) molds of brass (used as cold-finger) placed at the bottom to induce the unidirectional solidification of the slurries from the bottom to the top. All samples were frozen from room temperature to $-30\text{ }^\circ\text{C}$ in a Deep freezer (Remi ULT90). After freezing, the samples were carefully ejected and freeze dried at $-55\text{ }^\circ\text{C}$ and

666 mPa vacuum pressure in a freeze drier (SIM International FD5) for 24 h to sublime the solvent. A schematic of the water-based freeze-casting process for porous NKNS piezoelectric ceramics is shown in Fig. 1. Subsequently, the binder was burnt off at $650\text{ }^\circ\text{C}$, and the samples were sintered at $1140\text{ }^\circ\text{C}$ for 3 h in a closed alumina crucible in the air using a conventional electrical heating furnace. Simultaneously, similar samples were sintered at $1080\text{ }^\circ\text{C}$ for 1 h in a microwave-sintering furnace (VB Ceramic) with a heating rate of $20\text{ }^\circ\text{C}/\text{min}$, followed by natural cooling to room temperature.

The influence of the porosity gradient of sintered samples was ascertained by dividing it into three parts, viz., bottom (B), top (T), and middle (M), and samples were cut from each part using a high-precision slicing machine (Chennai Metco). Conventional- and microwave-sintered samples were labeled as C and M, respectively, and to identify different samples, abbreviations shown in Table 1 have been used throughout this paper.

A rheometer (Anton PaarPhysica MCR101) was utilized to measure the slurry's viscosity at various shear rates. The phase formation of calcined powder was analyzed using an X-ray diffractometer (Bruker D8 advance). A monochromatic X-ray source of Cu $K\alpha$ radiation ($\lambda \approx 1.5406\text{ \AA}$) was used with 40 kV/40 mA of power. The XRD patterns were collected in the range of 20° – 80° using the step-scanning mode with a step of 0.02° in 2θ and 50 s of step counting time. The microstructure of the calcined powder and porous morphology of the sintered samples was investigated using FESEM (Carl Zeiss – Merlin compact), and elemental analysis was carried out using AZTec software. Quantimet software was employed for grain size measurement. The particle size of the powder was examined using a laser particle size analyzer (Horiba LA-960). The density was calculated by measuring its mass and physical dimensions. The porosity of the porous ceramic is calculated using Eq. 1.

$$\text{Porosity}\% = \left[1 - \frac{\rho_{\text{real}}}{\rho_{\text{bulk}}} \right] \times 100, \quad (1)$$

where ρ_{real} and ρ_{bulk} are respectively, real and bulk density of ceramics ($\rho_{\text{bulk}} = 4.5\text{ gm}/\text{cc}$).

For the electrical measurements, silver electrodes were applied to both the surfaces of the sintered samples. Poling of the sample was carried out using corona poling as well as conventional silicon oil bath

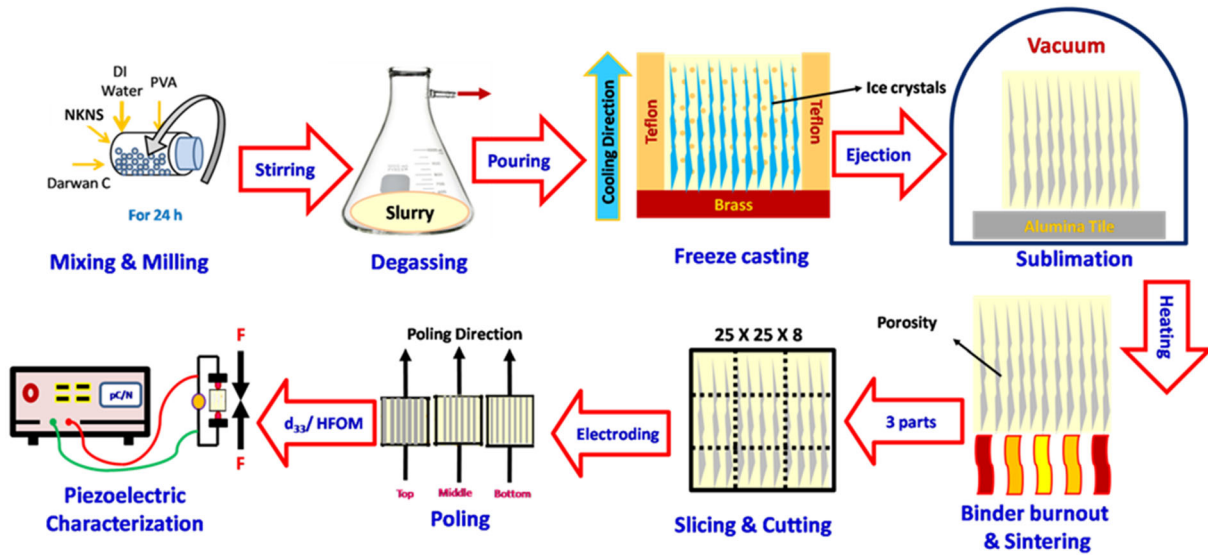


Fig. 1 Schematic of the preparation of the freeze-cast porous NKNS piezoceramic samples

Table 1 Sample abbreviation based on position and sintering methods

Position of the sample with respect to its cooling direction	Dimensions of the position with respect to height	Abbreviation	
		Conventional sintered (C)	Microwave sintered (M)
Bottom (B)	0–7 mm	NKNS-B-C	NKNS-B-M
Middle (M)	8–16 mm	NKNS-M-C	NKNS-M-M
Top (T)	17–24 mm	NKNS-T-C	NKNS-T-M

technique by applying an electrical field of 3 kV/mm in corona poling (Milman) at 80 °C for 45 min and 2 kV/mm in conventional poling at 110 °C for 45 min using high DC power supply (Glassman). Capacitance and dielectric constant were measured using LCR HiTester (HIOKI 3532, Japan). The piezo d_{33} meter (Piezotest PM300) was engaged to measure piezoelectric charge coefficient (d_{33}), and the same instrument was used for carrying out the thermal annealing study by measuring the d_{33} at different temperatures from 30 to 240 °C with a gap of 30 °C between each temperature reading after poling. The hydrostatic figure of merit (HFOM) of the poled sample was calculated by measuring the hydrostatic piezoelectric strain coefficient (d_h) and the hydrostatic piezoelectric voltage coefficient (g_h) values [7] using the following formulas:

$$d_h = d_{33} + 2d_{31}, \tag{2}$$

$$g_h = \frac{d_h}{\epsilon_0 \epsilon_r}, \tag{3}$$

$$HFOM = d_h \times g_h, \tag{4}$$

where (d_{33}) the longitude piezoelectric charge coefficient, (d_{31}) the transverse piezoelectric charge coefficient, (ϵ_0) the permittivity of free space, and (ϵ_r) the relative permittivity of ceramic. Aging of the samples is calculated using Eq. (5):

$$Aging\% = \left[\frac{(P_T - P_0)}{P_0} \right] \times \left[\log \left(\frac{T_T}{T_0} \right) \right] \times 100, \tag{5}$$

where T_0 , T_T , P_0 , and P_T are the starting time, aging time, properties at T_0 , and properties after aging for time T , respectively.

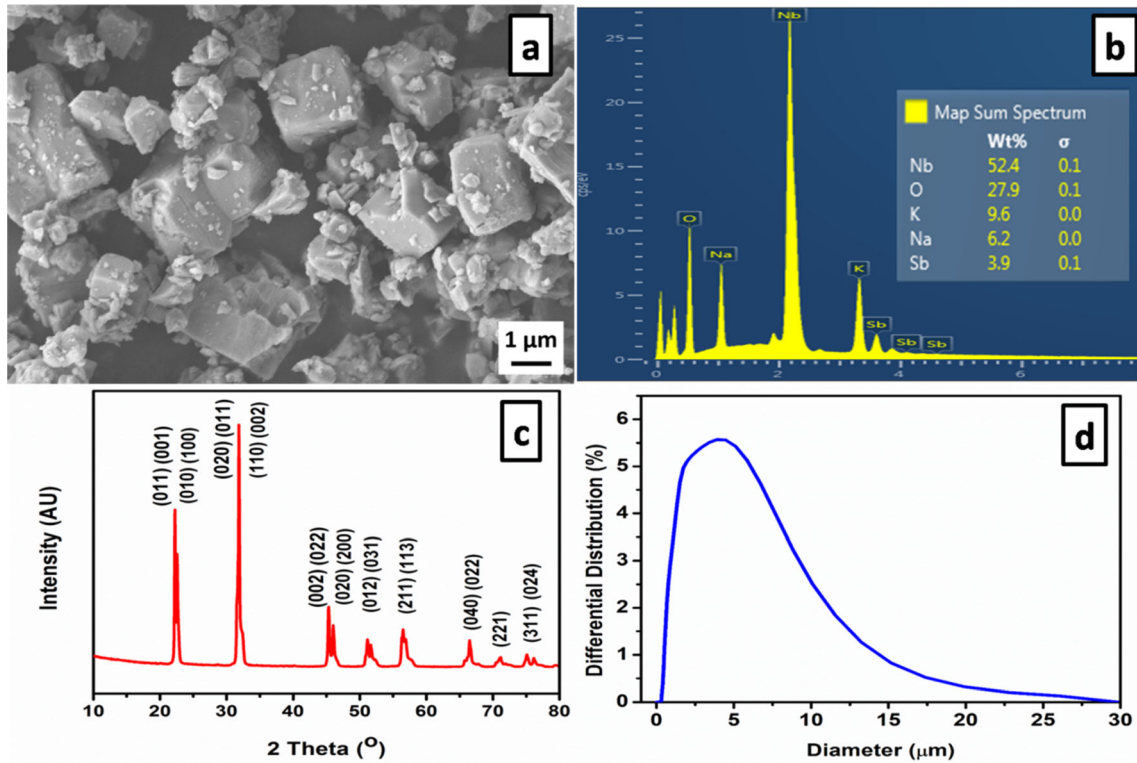


Fig. 2 **a** FESEM image, **b** EDX pattern, **c** X-ray diffraction profile, and **d** particle size distribution of NKNS ceramic powder calcined at 800 °C

3 Results and discussions

Figure 2a shows the scanning electron microscopy image of the as-synthesized NKNS powder. The NKNS powder exhibited an irregular sized and nearly cubical particle nature with smaller particles of 0.4–0.6 μm surrounding the bigger particles of around 2 μm, and the corresponding EDX results are shown in Fig. 2b. Theoretical percentage of Na, K, Nb, Sb and, O in calcined NKNS[(Na_{0.52}K_{0.48})(-Nb_{0.95}Sb_{0.05})O₃] powder are 6.91, 10.85, 51, 3.52 and, 27.73%, respectively, which are in good agreement with elemental results obtained through EDX. The X-ray diffraction profile of NKNS powder calcined at 800 °C is shown in Fig. 2c, which depicts the pure perovskite phase formation without any secondary or irrelevant phase with standard JCPDS NKNS card no. is. [32-0822]. The crystal structure of the calcined powder is found to be a polymorphic phase boundary having orthorhombic (*Amm*2) (JCPDS card no 01-071-2171) and tetragonal (*P4mm*) phases (JCPDS card no 01-071-0945). The particle size distribution of the NKNS powder is shown in Fig. 2d. The *d*₅₀ of the

particles is 3.27 μm, which is in correlation with SEM results.

Figure 3 exhibits the rheological properties of the as-prepared NKNS slurry, depicting the variation of flow behavior in response to applied stress. The slurry exhibited shear-thinning behavior as the

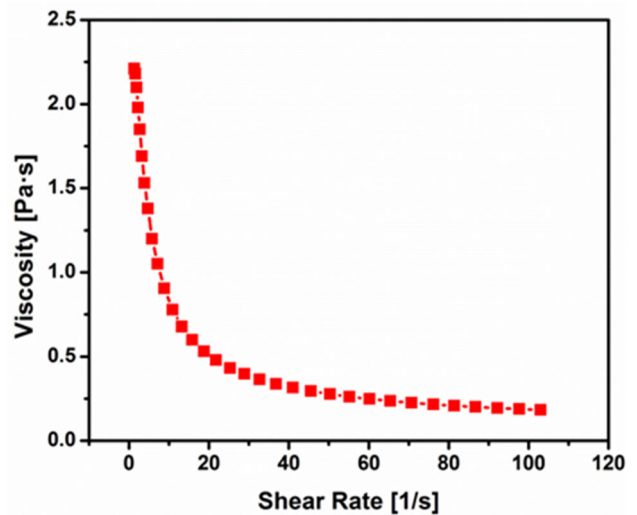


Fig. 3 Dependency of the 70 wt% NKNS slurry viscosity w.r.t shear rate

viscosity of slurry decreased with the increase in shear rate. Viscosity attains a stable value when the shear rate is around 80 s^{-1} . It has been reported that a minimal resistance to the breakdown of primary structures and aligning particles in the colloidal system can be achieved by shear-thinning behavior [35]. Figure 4a and b shows the variation of relative density (%) and porosity (%), respectively, of the conventional-, as well as a microwave-sintered porous NKNS samples with respect to sample position. Based on previous reports, microwave- and conventional-sintering temperatures of $1080 \text{ }^\circ\text{C}$ [36, 37] and $1140 \text{ }^\circ\text{C}$ [33, 34] were selected. As shown in Fig. 4a, the microwave-sintered samples were found to have a marginally higher relative density (1–3%) compared to conventional sintering because of the dielectric and

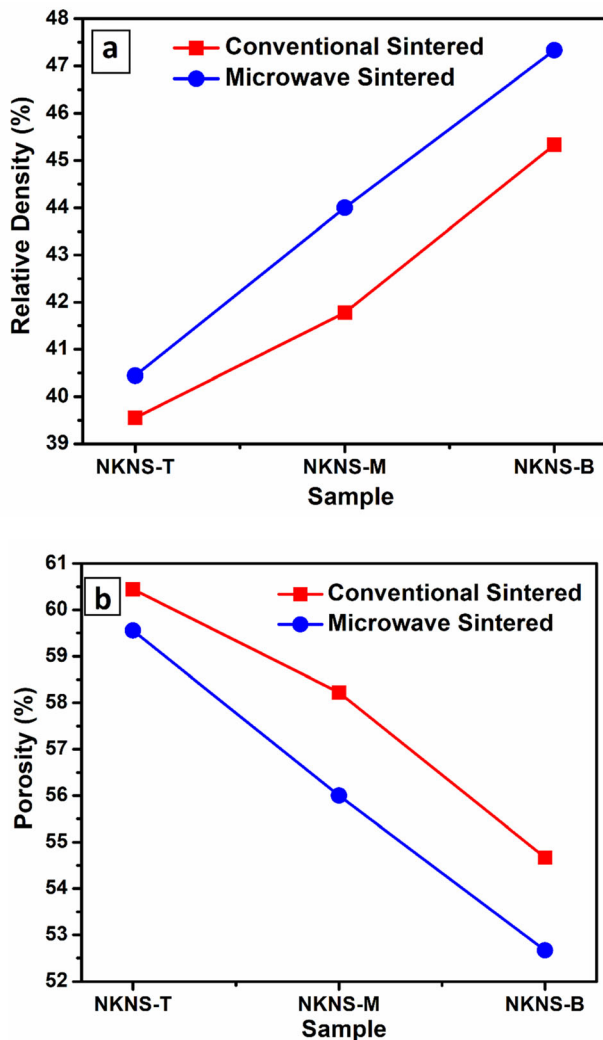


Fig. 4 **a** The relative density and **b** the porosity of various freeze-casted porous NKNS ceramics

resistant heating of the NKNS samples. A slight porosity gradient has also been observed in the samples from top to bottom, resulting in a porosity difference of 6–8% as shown in Fig. 4b. However, the settling of particles was not observed in the slurry. Consequently, NKNS-B-M sample holds the highest density (2.13 g/cc) and low porosity (52.67%), while NKNS-T-C displayed the highest porosity ($\sim 60.5\%$).

High-resolution FESEM images of conventional- and microwave-sintered freeze-cast porous samples in a direction parallel to the freezing direction are shown in Fig. 5. Highly aligned, closely packed lamellar structure morphology has been observed in all the samples. Aligned lamellar pore channels and ceramic structures are replicas of the orientated growth of the ice crystals [31]. Average dense ceramic wall thicknesses in NKNS-B-C, NKNS-M-C, and NKNS-T-C samples are 48, 93, and $141 \mu\text{m}$, respectively, under the $\times 250$ magnification. Predominantly, bimodal grain size distribution with smaller grains of $\sim 0.5 \mu\text{m}$ and larger grains of $\sim 1.5 \mu\text{m}$ is noticed in all the conventional-sintered samples under the $\times 10 \text{ K}$ magnification. The lamellas are found to be interconnected with a partial dendritic structure formed due to the tipping of ice crystals.

Similarly, average dense ceramic wall thicknesses in NKNS-B-M, NKNS-M-M, and NKNS-T-M samples are 50, 119, and $167 \mu\text{m}$, respectively, under the $\times 250$ magnification. Compared to conventional-sintered samples, there is a slight difference in wall thickness in the microwave-sintered sample, but a highly aligned grain structure with a sharp grain boundary is observed. Bimodal grain size distribution with fine grains of average size $0.7 \mu\text{m}$ and coarse grains of average size $2 \mu\text{m}$ is noticed in NKNS-T-M sample while grain size of $2.5\text{--}3 \mu\text{m}$ is observed in the other two samples under the $\times 10 \text{ K}$ magnification. Results of relative density and porosity concerning sample segments are well correlated with microstructure.

The effect of conventional poling and corona poling studies on the piezoelectric coefficient (d_{33}) of freeze-cast porous NKNS samples is shown in Fig. 6. It is pertinent here to mention that the materials with higher porosity will reduce piezoelectric properties due to the absence of the active ceramic phase [11]. Consequently, as expected, the porous NKNS-B-M sample sintered by the microwave method gives the piezoelectric charge coefficient (d_{33}) value of about 130 pC/N , which is about 6% higher than the value

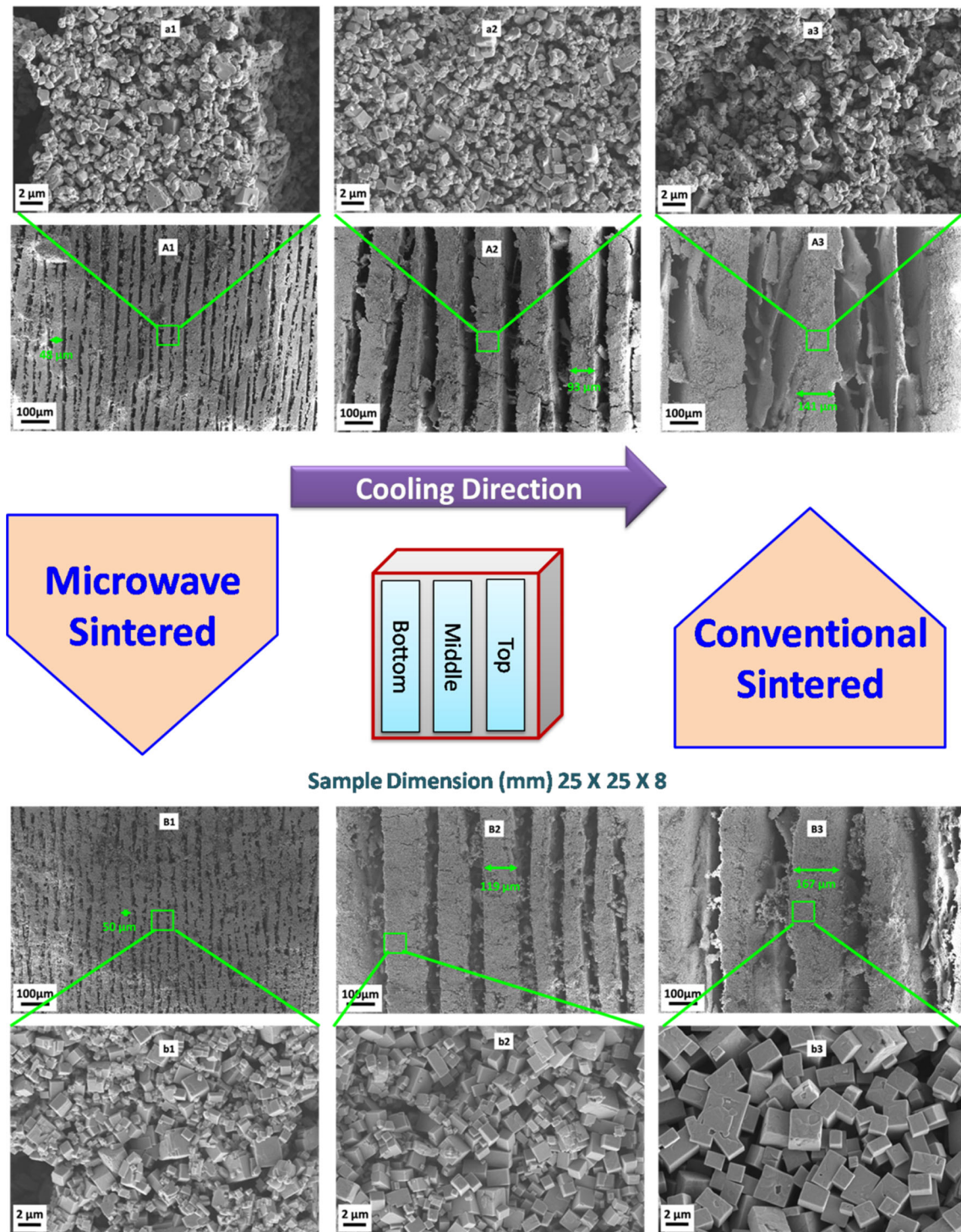


Fig. 5 FESEM microstructures ($\times 10$ K magnification) of porous NKNS ceramics with cross section parallel to the cooling direction, **a1** NKNS-B-C, **a2** NKNS-M-C, **a3** NKNS-T-C, **b1** NKNS-B-M, **b2** NKNS-M-M, **b3** NKNS-T-M [A1–A3, B1–B3 Magnification at $\times 250$]

of porous NKNS-B-C (d_{33} :122 pC/N) sintered by the conventional method; this is due to the microwave-sintering samples are having better alignment of the domains and a dense ceramic walls with improved

microstructure. The value of the piezoelectric coefficient reported in dense ceramic [33, 34] is retained even after possessing $\sim 50\%$ porosity in the sample. This peculiar behavior can be attributed to the

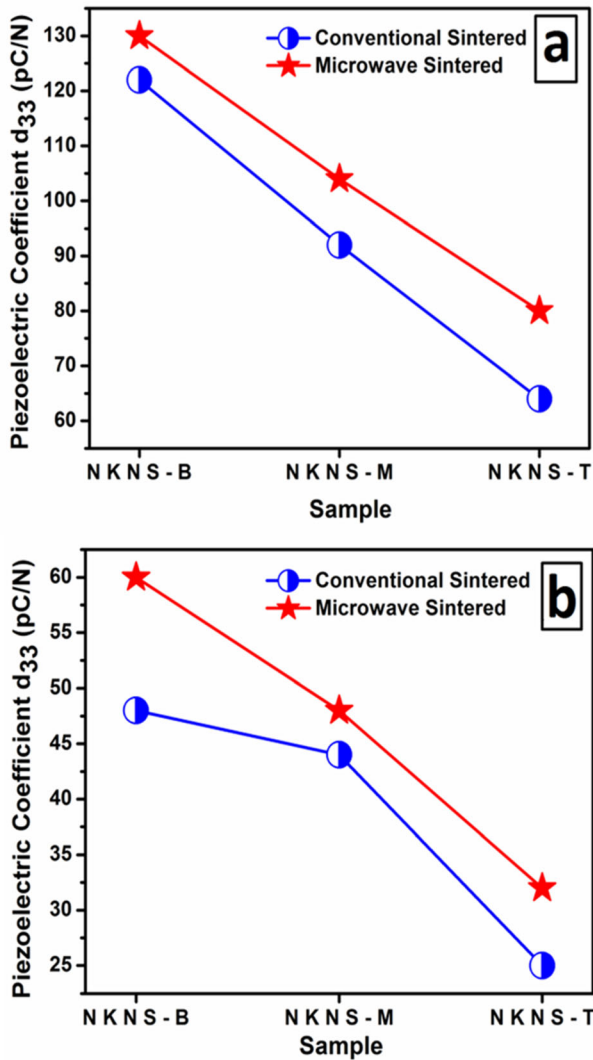


Fig. 6 Piezoelectric coefficient in longitudinal direction (d_{33}) of porous freeze-cast NKNS ceramics **a** conventional poled, **b** corona poled

following two factors: first, the highly aligned unidirectional lamellar structure obtained by freeze casting; second, as the sintering temperature and time are less, the volatilization of lighter elements is reduced, which may also have some influence on the properties. It can be deduced from the result that conventional poling is a better option than corona poling as more field is experienced by the sample leading to better domain wall switching and dipole alignment. Therefore, for further study, only conventional-poled samples of NKNS-B-M and NKNS-B-C are selected.

The aging and thermal stability behaviors of the selected samples are shown in Fig. 7a and b,

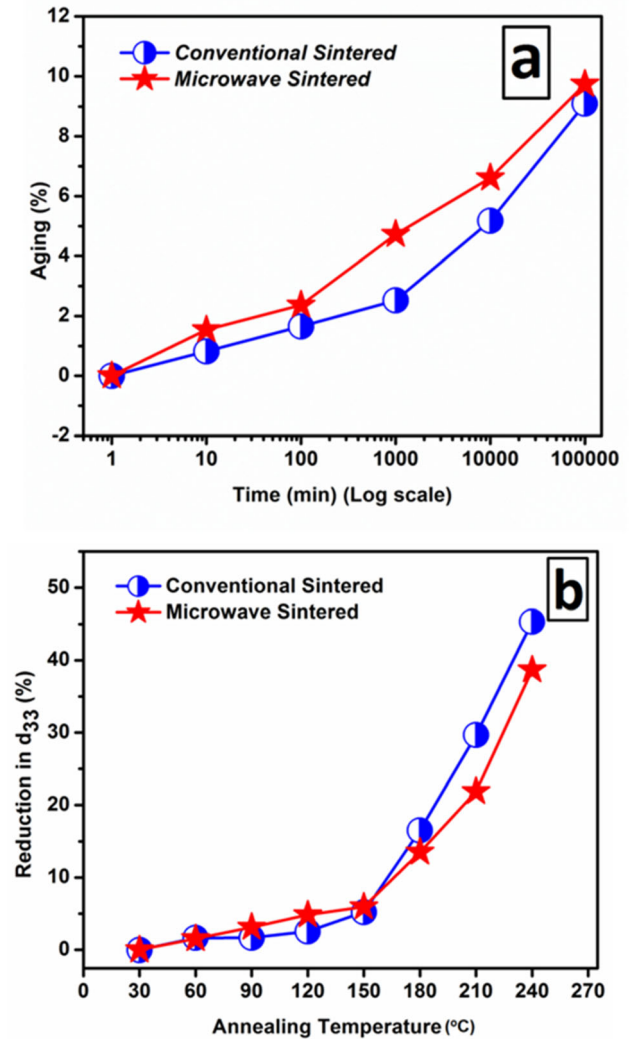


Fig. 7 **a** Aging behavior and **b** thermal stability of the porous freeze-casted NKNS-B ceramic

respectively. Aging is defined as the degradation of properties with time, in the absence of any mechanical or electrical load [38]. The fabricated samples display stable aging behavior, and the piezoelectric property does not deteriorate drastically with time. The influence of temperature on porous NKNS samples is studied by exposing samples at specific temperatures. A thermal annealing study shows that the NKNS ceramic is stable in terms of piezoelectric properties, even up to a temperature of 150 °C and the piezoconstant decreased only 4.5–5%, which is excellent from the application point of view. This behavior can be attributed to the higher Curie temperature (~ 320 °C) of NKNS composition depicting stability of domains that require higher thermal energy to perturb. Beyond this temperature, a slightly

Table 2 HFOM calculations of porous NKNS lead-free ceramic, ^ψ Dense NKNS ceramics prepared by cold pressing for comparison

Sample	d_{31} (pC/N)	Capacitance (pF)	Dielectric constant	d_h (pC/N)	g_h (mV m/N)	HFOM ($\times 10^{-15}$ Pa ⁻¹)
NKNS-B-C	– 31.0	11.68	115.5	60.0	58.70	3522
NKNS-B-M	– 35.8	12.75	125.9	58.4	52.35	3057
NKNS ^ψ	– 50.98	329	559.3	21.04	4.25	89

Table 3 Comparison of various physical, dielectric, piezoelectric, and hydrostatic parameters with different processing methods for lead-based and lead-free-based porous piezoelectric ceramics

Sr no.	Material	Process	Solid loading	Porosity (%)	g_h (mVm/N)	ϵ_r	HFOM (d_h, g_h) ($\times 10^{-15}$ pa ⁻¹)	Paper
1.	PZT	Starch consolidation	60 wt%	45	–	864	1800	[39]
2.	PZT-5H	Ionotropic gelation	10 wt%	56.8	–	1005	5597	[40]
3.	PZT-PZN	Camphene-based freeze casting	10 vol%	82	118	284	35,650	[11]
4.	PZT-5H	TBA-based freeze casting	57 vol%	45	11.78	800	2168	[8]
5.	PZT-5H	TBA-based freeze casting	15 vol%	68.7	28.3	1319	9648	[17, 41]
6.	PZT-5H	TBA-based freeze casting	15 vol%	57.6	–	502	22,299	[42]
7.	PZT-5H	TBA-based gel casting	10 vol%	58.6	50.58	446	10,117	[7]
8.	PZT	Water-based freeze casting	40 vol%	60	40.1	–	8260	[43]
9.	PZT-5H	Burps technique	80 wt%	80	54.2	316	8238	[15]
10.	PZT-5A	Burps technique	50 wt%	45	27	–	–	[13]
11.	PZT	Burps technique	50 wt%	45	47	–	2115	[44]
12.	PZT	Burps technique	60 vol%	52	9.54	620	500	[45]
13.	PZT-PCN	Burps technique	95 wt%	45.57	43.5	182	2732	[46]
14.	PZT	Burps technique	50 wt%	61	49	500	10,600	[47]
15.	PZT	Burps technique	90 wt%	33.8	31.1	671	5753	[48]
16.	PZT	Burps technique	87.5 wt%	41.5	42	330	5500	[49]
17.	PZT	Burps technique	–	45	72	160	7344	[50]
18.	LNKN	Egg albumen foaming	65 wt%	70	–	55	–	[51]
19.	BaTiO ₃	Water-based freeze casting	20 vol%	60	–	1282	–	[52]
20.	BCZT	Burps technique	52 wt%	25	10.2	1026	952	[53]
21.	NKN	Burps technique	40 vol%	40	–	–	–	[30]
22.	NKNS	Water-based freeze casting	70 wt%	54.5	58.70	115.5	3522	This Work

higher rate of degradation is observed within the studied temperature range.

In general, porous ceramics display low dielectric permittivity value due to a reduced fraction of the active piezoelectric ceramic phase, as reported in Table 2. In this study, among all porous samples, the NKNS-B-C achieved the lowest dielectric constant value (~ 116), which can be ascribed to the lower density compared to microwave-sintered samples. With the introduction of lamellar porosity, the hydrostatic strain coefficient value (d_h) marginally increased from 21.04 to 60 pC/N, as shown in Table 2, which was nearly three times higher than that of the dense sample. As the porosity was incorporated, the hydrostatic piezoelectric voltage constant (g_h) values remarkably increased from 4.25 to

58.70 mV m/N. Consequently, the NKNS-B-C sample shows the highest HFOM (3522×10^{-15} Pa⁻¹), which is significantly greater than some of the reported values, as shown in Table 3. Also, it is noted that the HFOM value of NKNS-B-C was nearly 39 times higher than that of the dense NKNS ceramic (89×10^{-15} Pa⁻¹). Development of porosity by freeze casting in lead-free NKNS piezoceramics resulted in a reduction of d_{31} value while retaining original d_{33} value. Thereby, the conventional-sintered sample shows improved HFOM compared to the microwave-sintered sample. The freeze-casted samples with different freezing vehicles exhibited comparable or even higher hydrostatic figure of merit than most other processing methods. It can be seen that freeze casting generally leads to high hydrostatic figures of

merit compared to other methods. Therefore, this work expands on porous lead-free NKNS ceramics' potential applications with the freeze-casting process and provides new opportunities for futuristic underwater transducer applications.

4 Conclusions

Highly oriented lamellar-structured lead-free NKNS piezoceramics were fabricated successfully for the first time. The study shows that freeze casting is an economical and easier method. Microwave sintering of porous ceramic results in improved densification with grain growth and a sharp cubic grain boundary compared to conventional sintering. This reduces not only sintering temperature but also the sintering time. The results suggested that even a slight variation in density may lead to a significant difference in properties. Comparison between corona poling and conventional polling suggested conventional poling as a better option for optimal properties. Moreover, because of the lamellar structure, the original value of the piezoelectric coefficient (d_{33}) is retained even after introducing more than 50% porosity in NKNS lead-free ceramic. NKNS-B-M sample displays the highest piezoelectric coefficient (130 pC/N) while the highest value of HFOM obtained in porous NKNS-B-C by this route is $3522 \times 10^{-15} \text{ Pa}^{-1}$.

Acknowledgements

The authors express their sincere gratitude to The Director, Armament Research and Development Establishment, Pune and Vice-Chancellor, Defence Institute of Advanced Technology, Pune, for extending their support for this work. Also, financial support from DRDO as SRF fellowship is acknowledged.

Compliance with ethical standards

Conflict of interest The authors declare that they have no conflict of interest.

References

- G.H. Haertling, J. Am. Ceram. Soc. (1999). <https://doi.org/10.1111/j.1151-2916.1999.tb01840.x>
- B. Jaffe, W.R. Cook Jr., H. Jaffe, *Piezoelectric Ceramics* (Academic Press, London and New York, 1971).
- E.U. Directive, Off. J. Eur. Union **L37**, 19 (2002)
- W. Bai, L. Wang, P. Zheng, F. Wen, L. Li, J. Zhai, Z. Ji, Ceram. Int. **44**, 16040 (2018)
- G. Hernandez-Cuevas, J.R. Leyva Mendoza, P.E. García-Casillas, C.A. Rodríguez González, J.F. Hernandez-Paz, G. Herrera-Pérez, L. Fuentes-Cobas, S.D. del Torre, O. Raymond-Herrera, H. Camacho-Montes, J. Adv. Ceram. (2019). <https://doi.org/10.1007/s40145-019-0314-8>
- K. Boumchedda, M. Hamadi, G. Fantozzi, J. Eur. Ceram. Soc. (2007). <https://doi.org/10.1016/j.jeurceramsoc.2007.02.124>
- A. Yang, C.A. Wang, R. Guo, Y. Huang, C.W. Nan, J. Am. Ceram. Soc. (2010). <https://doi.org/10.1111/j.1551-2916.2009.03585.x>
- T. Xu, C.A. Wang, J. Am. Ceram. Soc. (2014). <https://doi.org/10.1111/jace.12793>
- M. Xie, Y. Zhang, M.J. Krasny, C. Bowen, H. Khanbareh, N. Gathercole, Energy Environ. Sci. (2018). <https://doi.org/10.1039/c8ee01551a>
- Y. Zhang, L. Chen, J. Zeng, K. Zhou, D. Zhang, Mat. Sci. Eng. (2014). <https://doi.org/10.1016/j.msec.2014.02.022>
- S.H. Lee, S.H. Jun, H.E. Kim, J. Am. Ceram. Soc. (2007). <https://doi.org/10.1111/j.1551-2916.2007.01834.x>
- A.N. Rybyanets, Ferroelectrics (2011). <https://doi.org/10.1080/000150193.2011.594751>
- B.P. Kumar, H.H. Kumar, D.K. Kharat, J. Mater. Sci. Mater. Electron. (2005). <https://doi.org/10.1007/s10854-005-3746-6>
- C.R. Bowen, A. Perry, A.C.F. Lewis, H. Kara, J. Eur. Ceram. Soc. (2004). [https://doi.org/10.1016/S0955-2219\(03\)00194-8](https://doi.org/10.1016/S0955-2219(03)00194-8)
- H. Kara, R. Ramesh, R. Stevens, C.R. Brown, IEEE Trans. Ultrasound Ferroelectr. Freq Control (2003). <https://doi.org/10.1109/TUFFC.2003.1193622>
- D.P. Skinner, R.E. Newnham, L.E. Cross, Mater. Res. Bull. (1978). [https://doi.org/10.1016/0025-5408\(78\)90185-X](https://doi.org/10.1016/0025-5408(78)90185-X)
- R. Guo, C.A. Wang, A. Yang, J. Am. Ceram. Soc. (2011). <https://doi.org/10.1111/j.1551-2916.2010.04294.x>
- B.P. Kumar, B. Rawal, K.M. Rajan, Def. Sci. J. (2018). <https://doi.org/10.14429/dsj.68.12315>
- M. Allahverdi, S.C. Danforth, M. Jafari, A. Safari, J. Eur. Ceram. Soc. (2001). [https://doi.org/10.1016/S0955-2219\(01\)00047-4](https://doi.org/10.1016/S0955-2219(01)00047-4)
- R.E. Newnham, D.P. Skinner, K.A. Klicker, A.S. Bhalia, B.R. Hardiman, T.R. Gururaja, Ferroelectrics (1980). <https://doi.org/10.1080/00150198008226063>
- E.D. Pinheiro, T. Deivarajan, Acta Phys. Pol. A (2019). <https://doi.org/10.12693/AphysPolA.136.555>
- T. Xu, C.A. Wang, Mat. Des. (2016). <https://doi.org/10.1016/j.matdes.2015.11.101>

23. Y. Zhang, Y. Bao, D. Zhang, C.R. Bowen, *J. Am. Ceram. Soc.* (2015). <https://doi.org/10.1111/j.jace13797>
24. Q. Wang, X. Chen, J. Zhu, B.W. Darvell, Z. Chen, *Mater. Lett.* (2008). <https://doi.org/10.1016/j.matlet.2008.03.024>
25. Q. Wang, Q. Chen, J. Zhu, C. Huang, B.W. Darvell, Z. Chen, *Mater. Chem. Phys.* (2008). <https://doi.org/10.1016/j.matchemphys.2007.12.022>
26. Q. Wang, J. Yang, W. Zhang, R. Khoie, Y.M. Li, J.G. Zhu, Z.G. Chen, *Int. J. Oral Sci.* (2009). <https://doi.org/10.4248/ijos.09005>
27. T. Xu, C.A. Wang, *J. Eur. Ceram. Soc.* (2016). <https://doi.org/10.1016/j.jeurceramsoc.2016.03.032>
28. J.I. Roscow, Y. Zhang, M.J. Krašny, R.W.C. Lewis, J. Taylor, C.R. Bowen, *J. Phys. D: Appl. Phys.* (2018). <https://doi.org/10.1088/1361-6463/aabc81>
29. R. Guo, J. Roscow, C.R. Bowen, H. Luo, Y. Huang, Y. Ma, K. Zhou, D. Zhang, *J. Mater. Chem. A* (2020). <https://doi.org/10.1039/C9TA11360F>
30. A.N. Reznichenko, M.A. Lugovaya, E.I. Petrova, N.A. Shvetsova, A.N. Rybyanets, *Ferroelectrics* (2019). <https://doi.org/10.1080/00150193.2019.1570018>
31. Y. Zhang, M. Xie, J. Roscow, Y. Bao, K. Zhou, D. Zhang, C.R. Bowen, *J. Mater. Chem. A* (2017). <https://doi.org/10.1039/C7TA00967D>
32. F. Bouville, E. Maire, S. Meille, B.V. Moortèle, A.J. Stevenson, S. Deville, *Nat. Mater.* (2014). <https://doi.org/10.1038/nmat3915>
33. B. Rawal, N.N. Wathore, B. Praveenkumar, H.S. Panda, *J. Mater. Sci.: Mater. Electron.* (2017). <https://doi.org/10.1007/s10854-017-7553-7>
34. H.S. Panda, B. Rawal, N.N. Wathore, B. Praveenkumar, *J. Eur. Ceram. Soc.* (2019). <https://doi.org/10.1007/s10832-019-00179-2>
35. G. Liu, PhD Thesis, The University of Birmingham, (2011) pp. 40–41
36. M.R. Bafandeh, R. Gharakhani, M.H. Abbasi, A. Saidi, J.S. Lee, H.S. Han, *J. Eur. Ceram. Soc.* (2014). <https://doi.org/10.1007/s10832-014-9951-z>
37. D.Y. Jeong, S.H. Lee, H.C. Song, K.H. Choi, J.H. Cho, *J. Kor. Phys. Soc.* (2011). <https://doi.org/10.3938/jkps.58.663>
38. H. Birol, D. Damjanovic, N. Setter, *J. Eur. Ceram. Soc.* (2006). <https://doi.org/10.1016/j.jeurceramsoc.2004.11.022>
39. C. Galassi, *J. Eur. Ceram. Soc.* **26**, 2951 (2006). <https://doi.org/10.1016/j.jeurceramsoc.2006.02.011>
40. W. Liu, L. Lv, Y. Li, Y. Wang, J. Wang, C. Xue, Y. Dong, J. Yang, *Ceram. Int.* (2017). <https://doi.org/10.1016/j.ceramint.2017.02.079>
41. R. Guo, C.A. Wang, A.K. Yang, J.T. Fu, *J. Appl. Phys.* (2010). <https://doi.org/10.1063/1.3525056>
42. A. Yang, C.A. Wang, R. Guo, Y. Huang, C.W. Nan, *Ceram. Int.* (2010). <https://doi.org/10.1016/j.ceramint.2009.09.022>
43. Y. Zhang, J. Roscow, M. Xie, C. Bowen, *J. Eur. Ceram. Soc.* (2018). <https://doi.org/10.1016/j.jeurceramsoc.2018.04.067>
44. B.P. Kumar, H.H. Kumar, D.K. Kharat, *Bull. Mater. Sci.* (2005). <https://doi.org/10.1007/BF02711235>
45. E. Roncari, C. Galassi, F. Craciun, C. Capiani, A. Piancastelli, *J. Eur. Ceram. Soc.* (2001). [https://doi.org/10.1016/S0955-2219\(00\)00208-9](https://doi.org/10.1016/S0955-2219(00)00208-9)
46. H.T. Naeem, *Mater. Today. Proc.* (2020). <https://doi.org/10.1016/j.matpr.2019.09.184>
47. S. Marselli, V. Pavia, C. Galassi, E. Roncari, F. Craciun, G. Guidarelli, *J. Acoust. Soc. Am.* (1999). <https://doi.org/10.1121/1.427091>
48. T. Zeng, X.L. Dong, H. Chen, Y.L. Wang, *Mater. Sci. Eng. B.* (2006). <https://doi.org/10.1016/j.mseb.2006.04.009>
49. T. Zeng, X.L. Dong, S.T. Chen, H. Yang, *Ceram. Int.* (2007). <https://doi.org/10.1016/j.ceramint.2005.09.022>
50. Y.C. Chen, S. Wu, *Ceram. Int.* (2004). [https://doi.org/10.1016/S0272-8842\(03\)00064-6](https://doi.org/10.1016/S0272-8842(03)00064-6)
51. C. Chen, Y. Zhu, J. Ji, F. Cai, Y. Zhang, N. Zhang, A. Wang, *Mater. Res. Express.* (2018). <https://doi.org/10.1088/2053-1591/aaabe2>
52. G. Liu, T.W. Button, D. Zhang, *J. Eur. Ceram. Soc.* (2014). <https://doi.org/10.1016/j.jeurceramsoc.2014.05.043>
53. Y. Zhang, M. Xie, J. Roscow, C. Bowen, *Mater. Res. Bull.* (2018). <https://doi.org/10.1016/j.materresbull.2018.08.031>

Publisher's Note Springer Nature remains neutral with regard to jurisdictional claims in published maps and institutional affiliations.